Journal of Materials Chemistry A

ROYAL SOCIETY OF CHEMISTRY

PAPER

View Article Online
View Journal | View Issue

Cite this: J. Mater. Chem. A, 2024, 12, 7227

Modulating coal-derived carbon toward electrocatalytic generation of hydroxyl radicals for organic contaminant removal†

Guoqiang Zhao, [abc] Tianci Chen,[abc] Aidong Tang [*abcd] and Huaming Yang [*abce]

The three-electron oxygen reduction reaction (3e⁻ ORR), which consists of the electrochemical production of hydrogen peroxide (H_2O_2) and the subsequent activation, allows for the facile generation of hydroxyl radicals (˙OH) for environmental remediation. However, the current understanding on designing the corresponding electrocatalyst is not adequate. Herein, carbon-based electrocatalysts are prepared using bituminous coal as the raw material to obtain a high content of oxygen, which is crucial for H_2O_2 production, and the oxygen-containing functional groups (OFGs) in the electrocatalyst are modulated to improve the ˙OH production efficiency. Experimental and calculation results demonstrate that C=O groups serve as active sites for not only H_2O_2 formation but also the activation of H_2O_2 to produce ˙OH, while H_2O_2 desorption and H_2O_2 activation are more favorable at COOH and C=O sites, respectively. Therefore, after deliberately removing COOH groups from the coal-derived carbon surface, the ˙OH production efficiency is increased, leading to the fast removal of organic dyes from water. Our results demonstrate the significance of modulating the surface OFGs on the carbon-based electrocatalyst toward efficient ˙OH production from the 3e⁻ ORR, which provides a green and sustainable route toward organic contaminant removal from water.

Received 16th November 2023
Accepted 13th February 2024

DOI: 10.1039/d3ta07082d

rsc.li/materials-a

1 Introduction

Organic contaminants are ubiquitous in water and pose significant threats to the environment and human health.[1,2] Therefore, efficient methods to remove organic pollutants from water are highly desirable for the preservation of the natural environment.[3,4] Advanced oxidation processes (AOPs) have been extensively explored for generating reactive oxygen species (ROS) to decompose organics.[5–8] Among various ROS, hydroxyl radicals (˙OH) can oxidize most organic pollutants efficiently and unselectively, without secondary pollution.[9,10] In particular, the Fenton reaction between Fe^{3+} and H_2O_2 has been widely used to generate ˙OH for treating organic contaminants.[11–13] However, the storage of H_2O_2 has potential safety hazards, and the use of Fe^{3+} may induce secondary pollution. Various heterogeneous Fenton reaction systems have been proposed to overcome the above shortcomings.[14,15] Recently, it has been demonstrated that ˙OH can be produced electrochemically by the three-electron ($3e^-$) oxygen reduction reaction (ORR).[16,17] In specific, O_2 can be reduced to H_2O_2 by the two-electron ($2e^-$) ORR,[18–22] and the obtained H_2O_2 molecules can be subsequently activated to ˙OH *via* a one-electron reduction process.[23,24] Together, this $3e^-$ ORR pathway enables the production of ˙OH without the use of Fe^{3+} and H_2O_2, and thus would solve the challenges facing the Fenton method fundamentally. The key here is developing an advanced electrocatalyst that can produce ˙OH from O_2 with high efficiency and selectivity.

For the $2e^-$ ORR, carbon-based electrocatalysts have shown attractive performance in recent studies,[25–28] and oxygen-containing functional groups (OFGs) such as carboxyl (COOH), epoxide (C–O–C), carbonyl (C=O), and hydroxyl (–OH) groups play a significant role in achieving high activity and selectivity.[29–31] To be specific, OFGs can create additional adsorption sites on the carbon surface, and hence increase the number of active sites for electrochemical reactions.[32–35] Meanwhile, OFGs may modulate the local electronic structures of the catalyst and regulate the free energy of OOH* adsorption (ΔG_{OOH*}),[30,36,37] which exerts a significant impact on the selectivity toward the ORR.[38] As for H_2O_2 activation, common heterogeneous catalysts include transition

[a]Engineering Research Center of Nano-Geomaterials of Ministry of Education, China University of Geosciences, Wuhan, 430074, China. E-mail: tangaidong@cug.edu.cn; hm.yang@cug.edu.cn

[b]Faculty of Materials Science and Chemistry, China University of Geosciences, Wuhan, 430074, China

[c]Laboratory of Advanced Mineral Materials, China University of Geosciences, Wuhan, 430074, China

[d]College of Chemistry and Chemical Engineering, Central South University, Changsha 410083, China

[e]Hunan Key Laboratory of Mineral Materials and Application, School of Minerals Processing and Bioengineering, Central South University, Changsha 410083, China

† Electronic supplementary information (ESI) available. See DOI: https://doi.org/10.1039/d3ta07082d

metals (TMs, *i.e.* Fe, Co, and Ni), TM oxides, or TM-based composite materials, and metal species are typical active sites.[39–41] Interestingly, recent studies have shown that carbon-based materials can also be used for activating H_2O_2, where OFGs also play a nonnegligible role.[16] Therefore, it is a promising strategy to develop efficient carbon-based electrocatalysts toward producing $^{\bullet}OH$ from O_2 by increasing the amount and modulating the type of OFGs. However, current understanding on the relation between the $^{\bullet}OH$ production efficiency and the electrocatalyst structure is not adequate.

In this work, coal-derived carbon (bitu@C) is prepared using bituminous coal as the raw material and is used for producing $^{\bullet}OH$ from O_2 to remove acid orange II (AOII) from water. Characterization results prove that the as-prepared bitu@C possesses a large amount of C–O–C and COOH groups due to the use of high oxygen-containing precursors, in sharp contrast to the low amount of OFGs in commercial carbon black (CB). Therefore, bitu@C shows high ORR activity and rapid AOII degradation performance. Furthermore, the COOH groups are deliberately removed from bitu@C *via* an annealing treatment, leading to the enhanced AOII degradation performance. Theoretical calculations prove that the adsorption of OOH* on COOH groups is weak, which leads to fast H_2O_2 desorption, while the electrochemical activation of H_2O_2 to produce $^{\bullet}OH$ is more favored on C=O groups. The annealing treatment induced the conversion of COOH to C=O groups, and therefore the enhanced $^{\bullet}OH$ production efficiency results in promoted AOII degradation kinetics. Our work not only demonstrates a straightforward method for developing oxygen-rich carbon-based electrocatalysts but also provides fundamental insights into the relation between the electrochemical generation of $^{\bullet}OH$ and OFGs. The results would stimulate the development of versatile, efficient, and environmentally compatible methods for removing organic contaminants, which is highly desirable for a green and sustainable society.

2 Experimental procedures

2.1 Materials preparation

2.1.1 Chemicals. Raw bituminous coal powders were produced in the Shanxi province in China and were purchased from Henan Zhengzhou Long Yue Filter Material Co., Ltd. Anhydrous ethanol (EtOH), KOH, and H_2SO_4 were purchased from Sinopharm. Commercial CB was purchased from Nanjing Sunbio Technology Co., Ltd. Disodium terephthalate (TPA) and Nafion 117 solution (5% w/w in water and 1-propanol) were purchased from Shanghai Macklin Biochemical Technology Co., Ltd. Anhydrous Na_2SO_4 and acid orange II (AOII) were purchased from Shanghai Aladdin Agent Co., Ltd. Ultrapure deionized water (DIW, 18 MΩ cm^{-1}) was used in all the experiments. All chemicals were used as received without further purification.

2.1.2 Preparation of bitu@C. Coal-based carbon (bitu@C) was prepared by pyrolyzing bituminous coal powders in the presence of KOH. In a typical synthetic process, 5 g KOH was dissolved in 50 mL EtOH, and then 2.5 g raw bituminous coal powders were added to the above solution, and treated with ultrasonication for 2 h. Then, EtOH was evaporated in an electric oven at 80 °C for 4 h, and the obtained powders were placed in a porcelain boat and calcined at 800 °C under a N_2 atmosphere for 90 min. After cooling to room temperature, the sample was dispersed in 2 M H_2SO_4 and treated with ultrasonication for 1 h. Finally, the samples were washed with DIW and EtOH several times, and were collected by centrifugation and dried at 80 °C for 12 h.

2.1.3 Preparation of aCB. The aCB sample was prepared *via* a similar procedure to that of bitu@C, except that commercial CB was used to replace bituminous coal.

2.1.4 Preparation of bitu@C-300 and bitu@C-800. The bitu@C-300 and bitu@C-800 samples were prepared by annealing the as-prepared bitu@C under a nitrogen atmosphere at 300 and 800 °C for 2 h, respectively.

2.2 Material characterization

X-Ray diffraction (XRD) patterns were recorded on a Bruker D8 Advance (Germany) with CuKα radiation (40 kV, 130 mA, λ = 0.15406 nm) at a scan rate of 5° min^{-1}. Transmission electron microscopy (TEM) images were obtained on a JEM-2100 microscope operating at a working voltage of 200 kV. The specific surface area was analyzed on a Micromeritics TriStar II PLUS by using N_2 adsorption–desorption isotherms using the Brunauer–Emmett–Teller (BET) method. The pore distributions were calculated by the non-local density functional theory method. Raman spectra were collected on a Horiba LabRAM HR Evolution (Japan) with a laser wavelength of 633 nm. X-ray photoelectron spectra (XPS) were recorded on a Thermo Fisher K-alpha XPS spectrometer (America), which employed monochromatic AlKα radiation as the X-ray source. Thermogravimetric (TG) analysis was conducted on a NETZSCH STA449 thermogravimetric analyzer (Germany). The samples were treated under a nitrogen atmosphere from 25 to 800 °C with a heating rate of 5 °C min^{-1}.

2.3 Electrochemical performance measurements

All electrochemical test data were recorded using a computer-controlled CHI660D electrochemical workstation. The ORR electrocatalytic performance of the samples was studied in a typical three electrode system, where a carbon rod and an Hg/HgO electrode were used as the counter and the reference electrode, respectively. All obtained potentials were calibrated to the reversible hydrogen electrode (RHE). The catalyst was coated on the surface of a rotating disk electrode (RDE, 0.196 cm^2, Pine Research Instrumentation, US) and then used as the working electrode. Typically, 10 mg as-prepared catalyst and 20 μL Nafion solution (5 wt%) were dispersed in a solution mixture containing 300 μL DI water and 700 μL EtOH, and treated with ultrasonication for 2 h. Then 5 μL of the catalyst ink was drop-cast onto the RDE, and dried naturally at room temperature. The electrolyte was O_2-saturated 0.05 M Na_2SO_4 solution, and the pH was adjusted to 10 using 0.1 M KOH solution. Linear sweep voltammetry (LSV) curves were obtained at a scanning rate of 5 mV s^{-1} and a rotating speed of 1600 rpm. The selectivity of the $2e^-$ ORR was estimated with the RRDE test. The working electrode was prepared by similar procedures, and the

surface areas are 0.2472 and 0.1859 cm^2 for the disk and the ring of the used RRDE, respectively. The potential of the Pt ring electrode was set at 1.2 V *vs.* RHE for H_2O_2 detection. The H_2O_2 selectivity can be calculated by using the following equation:

$$H_2O_2\ (\%) = 200 \times \frac{\frac{I_R}{N}}{\left(I_D + \frac{I_R}{N}\right)}$$

where I_R is the ring current, I_D is the disk current, and N is the collection efficiency of the RRDE (0.37).

The kinetic current (I_K) is evaluated by using the Koutecký–Levich equation.

$$\frac{1}{I} = \frac{1}{I_K} + \frac{1}{I_D}$$

where I is the overall ORR current and I_D is the diffusion current.

The electron transfer number (n) is calculated by using the Levich equation

$$I_D = 0.62nF(D_0)^{\frac{2}{3}}(V)^{-\frac{1}{6}}\omega^{\frac{1}{2}}C_0$$

where F is the Faraday constant (96 485 C mol^{-1}), D_0 is the diffusion coefficient of oxygen (1.93×10^{-5} cm^2 s^{-1}), V is the dynamic viscosity of the solution (1.01×10^{-2} cm^2 s^{-1}), ω is the electrode rotation rate (rad s^{-1}), and C_0 is the volume concentration of oxygen (1.26×10^{-6} mol cm^{-3}).

For the H_2O_2 electrochemical activation measurement, LSV curves were first obtained in O_2-free 0.05 M Na_2SO_4 solution (pH = 10). Then, 0.48 mL of 30 vol% H_2O_2 solution was added to the above solution, and LSV curves of the samples were collected. The difference between the two LSV curves can be attributed to the H_2O_2 electrochemical activation.

For the detection of $^{\bullet}OH$, TPA is used as the probe, and the concentration of the fluorescent product hydroxyterephthalate (hTPA) was evaluated using ultraviolet-visible (UV-vis) spectroscopy.

2.3.1 Organic contaminant degradation measurement. The degradation of AOII was investigated in a three electrode system, where a carbon rod and an Hg/HgO electrode were used as the counter electrode and the reference electrode, respectively. For the preparation of the working electrode, a certain amount of catalyst ink was coated on the surface of the carbon cloth or ITO glass (working area: 1 cm^2), and the catalyst loading was controlled at 0.5 mg cm^{-2}. The electrolyte was 50 mL 0.05 M Na_2SO_4 solution containing 20 mg L^{-1} AOII, and the pH was adjusted to 10 using 0.1 M KOH. During the test, the electrolyte was continuously bubbled with O_2 under stirring, and the working potential was set at 0.2 V *vs.* RHE. After the predetermined time intervals, 1 mL of the electrolyte was taken and the concentration of AOII was determined by using an UV-vis spectrophotometer. The absorbance at 484 nm of standard AOII solutions with different concentrations was measured for the linear fitting of the AOII concentration.

2.4 Computational methods

All DFT calculations were performed using the Vienna *ab initio* simulation package (VASP).[42] The projector augmented wave (PAW)[43] pseudopotential with the PBE[44] generalized gradient approximation (GGA) exchange correlation function was utilized in the computations. The cutoff energy of the plane wave basis set was 500 eV and a Monkhorst–Pack mesh of $3 \times 3 \times 1$ was used in K-sampling in the calculation of adsorption energy and $9 \times 9 \times 1$ was used in the calculation of DOS. All structures were spin polarized and all atoms were fully relaxed with an energy convergence tolerance of 10^{-5} eV per atom, and the final force on each atom was <0.05 eV $Å^{-1}$.

The adsorption energy of reaction intermediates can be computed using the following eqn (1):

$$\Delta G_{ads} = E_{ads} - E_* + \Delta E_{ZPE} - T\Delta S \quad (1)$$

where ads = (O_2*, OOH*, O*, OH*), ($E_{ads} - E_*$) is the binding energy, ΔE_{ZPE} is the zero-point energy change, and ΔS is the entropy change. In this work, the values of ΔE_{ZPE} and ΔS were obtained by vibration frequency calculations.

The Gibbs free energy of the four reaction steps can be calculated by using the following four eqn (2)–(5):

$$* + O_2 + e^- + H_2O = *OOH + OH^- \quad (2)$$

$$*H_2O_2 + e^- = *OH + OH^- \quad (3)$$

$$*H_2O_2 = * + H_2O_2 \quad (4)$$

$$*OH + e^- = * + OH^- \quad (5)$$

3 Results and discussion

The bitu@C electrocatalyst was prepared using bituminous coal powders as the raw material. First, bituminous coal powders were mixed with KOH with a coal : KOH mass ratio of 1 : 2, and then were pyrolyzed under a N_2 atmosphere at 800 °C for 90 min (Fig. 1a). After acid washing and drying, the bitu@C samples were obtained. Commercial CB powders were also treated with a similar KOH activation method for reference, and the obtained sample was denoted as activated carbon black (aCB). Notably, the KOH treatment at high-temperature is commonly used to activate carbon materials owing to the violent reaction of KOH and carbon,[45,46] which would increase the amount of OFGs.

The obtained bitu@C exhibits a sheet-like morphology, as displayed in the transmission electron microscopy (TEM) image in Fig. 1b, while the morphology of CB does not show apparent changes after the KOH treatment (Fig. S1†). The X-ray diffraction (XRD) patterns demonstrate that there are a few mineral impurities including SiO_2 and kaolinite in the raw bituminous coal powders (Fig. 1c), and the thermogravimetric (TG) curve in Fig. S2a† indicates an ash content of 35.5%. During the preparation of bitu@C, KOH powders reacted with mineral impurities, and the resultant product could be readily removed by acid washing, and the ash content is dramatically reduced to 6.0%. Therefore, the obtained bitu@C sample shows typical features of amorphous carbon in the XRD patterns, similar to those for CB and aCB. The specific surface area (S_{BET}) and the

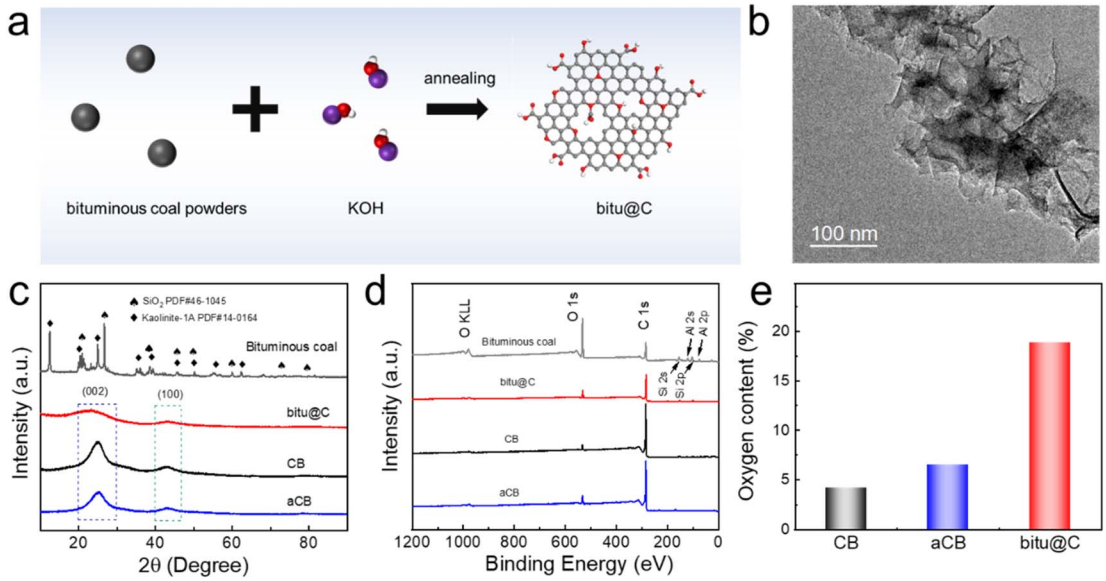

Fig. 1 (a) Illustration of the preparation of an oxygen-rich carbon electrocatalyst using bituminous coal as the raw material. (b) TEM image of the bitu@C sample. (c) XRD patterns of the samples. (d) XPS survey spectra of different samples. (e) Oxygen content of different samples.

pore size distribution of the samples were determined based on the nitrogen adsorption–desorption isotherm measurements using the Brunauer–Emmett–Teller (BET) theory (Fig. S3†). The S_{BET} of CB is slightly increased after KOH activation together with the increased pore volume and enlarged pore size, while bitu@C exhibits a much larger S_{BET} but a smaller average pore size (Table S1†). Furthermore, X-ray photoelectron spectroscopy (XPS) was employed to investigate the chemical states of the samples (Fig. 1d). In addition to C and O, there are also Si and Al elements in bituminous coal powders due to the presence of SiO_2 and kaolinite impurities. These impurities, however, are barely present in bitu@C. The oxygen content of bituminous coal powders is very high, and hence the obtained bitu@C shows a high oxygen content of up to 18.8% (Fig. 1e). In contrast, the oxygen content in CB is merely 4.2%, and is slightly increased to 6.5% after KOH activation. These results demonstrate that an oxygen-rich carbon-based electrocatalyst was successfully prepared from the pyrolysis of bituminous coal powders.

Textile dye wastewater is an important source of water pollution that is difficult to degrade.[47] Therefore, acid orange II (AOII) was used to evaluate catalytic performance of the carbon-based catalysts toward the $3e^-$ ORR. The measurement was performed using a three-electrode setup where catalysts coated on carbon cloth (CC) were employed as the working electrode. Details about the experiments can be found in the experimental section. Fig. 2a shows the concentration of AOII based on the treatment time. The AOII concentration is decreased by 38% after 1 h treatment using the bare CC as the working electrode, and the value is slightly increased to 43% and 47% for CB and aCB, respectively. In contrast, the concentration of AOII decreased by 73% at the end of the test using bitu@C. The degradation kinetics of AOII in the first 30 min was fitted by using the pseudo-first-order reaction, and the obtained apparent rate constant (k) is 0.034 min^{-1} for bitu@C (Fig. 2b), much higher than that of CB (0.014) and aCB (0.016). Meanwhile, the contribution of physical adsorption was also evaluated (Fig. S4†). The physical adsorption using bitu@C is slightly enhanced probably due to the increased specific surface area, but it cannot fully account for the substantially increased AOII degradation degree by the $3e^-$ ORR. Thus, the major contribution should be attributed to the electrochemically produced $^{\bullet}OH$ species. Detailed electrochemical measurements were performed to investigate the reason for the catalytic performance enhancement. First, the samples were coated on the surface of indium–tin oxide (ITO) conductive glass to exclude the influence of the CC substrate. The results in Fig. 2c also demonstrate the apparently higher degradation rate of bitu@C than that of CB and aCB. Second, the ORR activity of the samples and the corresponding selectivity toward the $2e^-$ ORR are evaluated using the rotating ring disk electrode (RRDE) measurement. In Fig. 2d, the disk current density (j_{disk}) illustrates the overall ORR activity of the samples, and the ring current density (j_{ring}) is derived from the oxidation of the generated H_2O_2. Thus, the selectivity toward the $2e^-$ ORR can be calculated, and the results are displayed in Fig. 2e. CB exhibits high selectivity toward the $2e^-$ ORR, but the overall activity is low. After KOH activation, the aCB shows improved ORR activity but decreased $2e^-$ ORR selectivity. As for bitu@C, the catalyst shows the highest overall ORR activity and the lowest $2e^-$ ORR selectivity. Third, linear sweep voltammetry (LSV) curves are obtained with and without the presence of H_2O_2 to evaluate the H_2O_2 electrochemical activation performance of the samples (Fig. 2f). The electrochemical H_2O_2 activation activity of bare CB is relatively low and is barely improved for aCB. In contrast, bitu@C exhibits substantially improved H_2O_2 activation performance. These results can explain the varied AOII degradation performances of different catalysts. In spite of the high

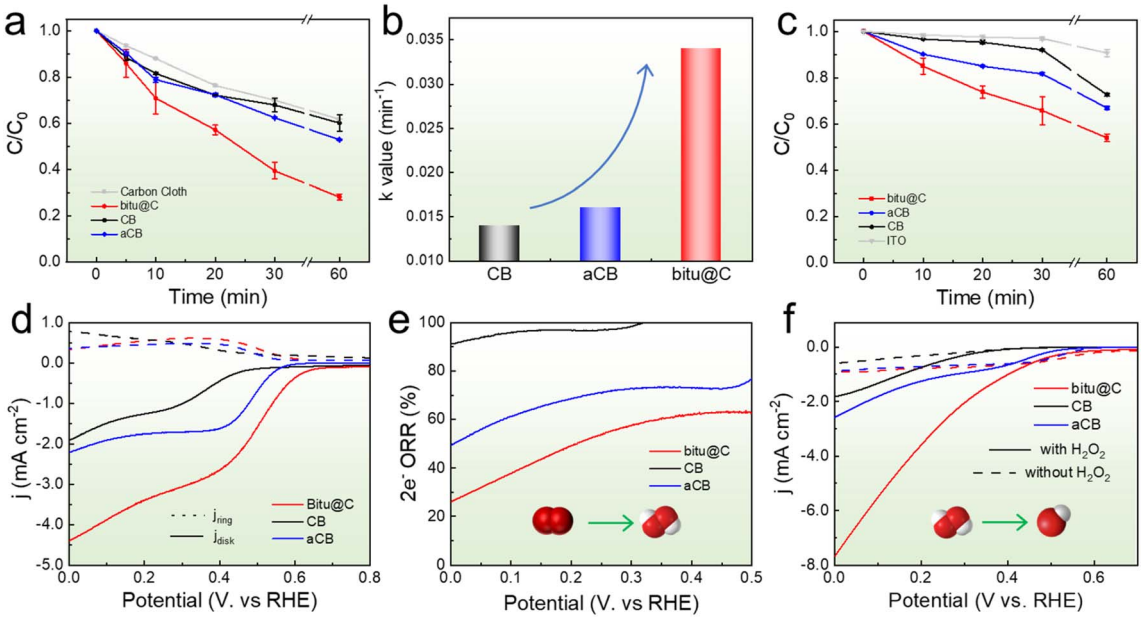

Fig. 2 Electrochemical performance of CB, aCB, and bitu@C. (a) Degradation of 20 mg L^{-1} AOII by the $3e^-$ ORR. Error bars are based on standard errors. (b) The calculated rate constant for the degradation of AOII using different catalysts. (c) Degradation of AOII using bitu@C as the catalyst (conductive glass as the substrate). (d) The polarization curves measured by using a rotating ring disk electrode (RRDE). (e) The calculated selectivity toward the $2e^-$ ORR based on the polarization curves. (f) Polarization curves with and without the presence of H_2O_2, demonstrating the H_2O_2 electrochemical activation performance.

$2e^-$ ORR selectivity, bare CB exhibits low ORR activity, and the produced H_2O_2 cannot be activated efficiently, thereby leading to the poor AOII degradation performance. As for aCB, although the ORR activity is somewhat increased, the H_2O_2 electrochemical activation is not improved, and hence the AOII degradation performance is barely changed. The increased overall ORR activity of aCB should be attributed to the increased selectivity toward the $4e^-$ ORR. When it comes to bitu@C, the above electrochemical measurements demonstrate high ORR activity with balanced H_2O_2 production and H_2O_2 activation performance, which leads to the rapid generation of $^{\bullet}OH$ and hence the fast AOII degradation.

In addition to the produced $^{\bullet}OH$ species *via* the $3e^-$ ORR, there are two additional potential reasons for AOII degradation, *i.e.*, the direct oxidation of AOII and the generation of $^{\bullet}OH$ *via* the $2e^-$ water oxidation reaction at the anode side. In particular, carbon-based materials have great promise for the $2e^-$ water oxidation reaction.[48] The working potential of the carbon rod plays a central role in both cases. Therefore, the LSV curve of the carbon rod electrode is obtained to evaluate the electrode potential at the anode side during the reaction (Fig. S5†). Then, the contribution of the direct oxidation of AOII and the two-electron water oxidation reaction at the anode side are evaluated by holding the carbon rod electrode at a specific electrode potential without O_2 bubbling. As shown in Fig. S6,† the contributions of the anode are 5.7%, 11.5%, and 20.2% at a working potential of 1.5, 1.7, and 1.9 V in 30 min, respectively. During the AOII degradation measurement, the typical working current of the catalysts is 2–4 mA, while the electrode potential of the carbon rod is 1.50 V at a working current of 5 mA. These results indicate that the contribution of the anodic oxidation of AOII and the $2e^-$ water oxidation to AOII degradation is small in our case but cannot be neglected at higher electrode potentials.

Detailed structure characterization studies were performed to provide insights into the role of OFGs in the $3e^-$ ORR. Fig. 3a and b show the TG and differential thermal analysis (DTA) results, respectively, where the mass loss of carbon materials is mostly derived from the removal of adsorbed water and the decomposition of OFGs.[49,50] The CB catalyst shows no significant mass loss up to 800 °C, while the mass loss is increased to 13.5% for aCB. Noteworthily, the mass loss of bitu@C reaches as high as 40% at 800 °C, highlighting the obvious variations in the surface structure. The peak between 0–150 °C in the DTA curve for bitu@C can be ascribed to the removal of the adsorbed water which accounts for a mass loss of 15.3%. Another well-defined peak can be observed between 150 and 350 °C for bitu@C, which is not present in either CB or aCB. This peak is mainly derived from the pyrolysis of COOH groups,[51] and contributes to a mass loss of 17.1%. In the temperature region higher than 350 °C, the mass loss can be attributed to the decomposition of C–O–C, OH, and C=O groups.[51] The TG and DTG results demonstrate that bitu@C possesses a higher content of OFGs, *i.e.* mostly COOH groups, compared with CB and aCB. The Raman spectra in Fig. 3c demonstrate the similar degrees of graphitization for CB, aCB, and bitu@C. Furthermore, near-edge X-ray absorption fine structure (NEXAFS) spectra of the samples at the O–K edge are obtained to provide insights into the electronic structure of the samples. As displayed in Fig. 3d, the peaks located at 530.0–535.5 eV are ascribed to the π* excitation of C=O, and the peaks at 537.5–

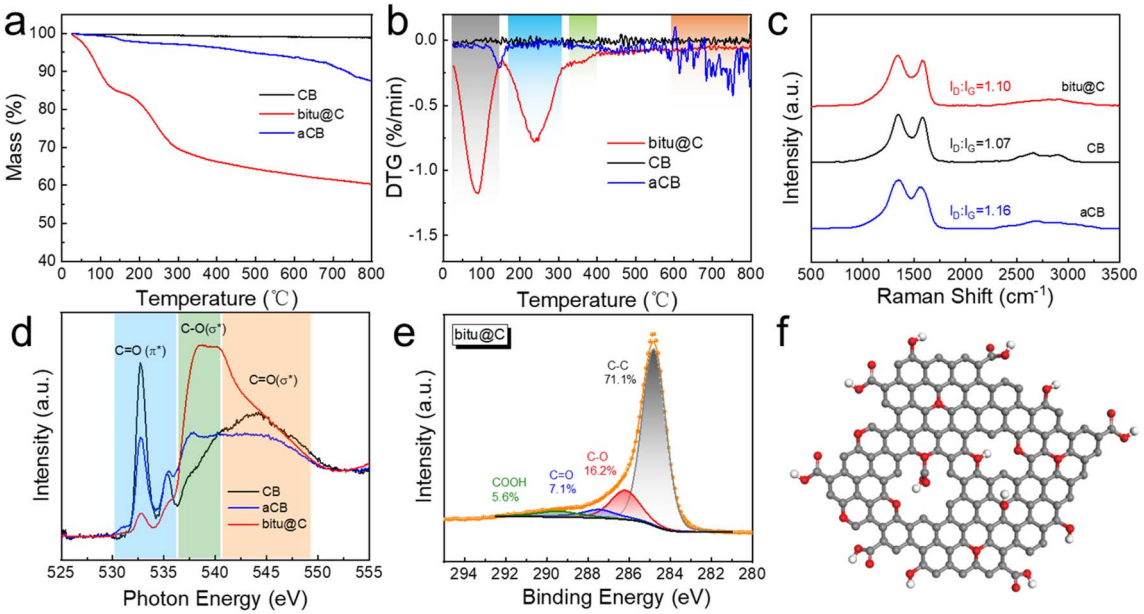

Fig. 3 Structure characterization of the samples. (a) TGA analysis, (b) DTG analysis, (c) Raman spectra, and (d) NEXAFS of CB, aCB, and bitu@C. (e) High-resolution C 1s XPS spectra of bitu@C. (f) Illustration of the structure of bitu@C.

540 eV and 541.5–548.0 eV correspond to the σ* excitation of C–O and the σ* excitation of C═O, respectively.[52,53] The results indicate that the major OFG in CB is COOH and C═O groups, and more C–O groups are found after KOH activation. As for bitu@C, the spectra show a prominent peak for C–O(σ*), consistent with the XPS and TG results that additional COOH and C–O–C groups are formed in bitu@C. High-resolution XPS spectra are analyzed to explore the electronic states of C and O. The C 1s XPS spectra of CB and aCB are shown in Fig. S7 and S8,† respectively. The fitting results demonstrate the increased C–O containing groups and the decreased C═O containing groups after KOH activation. Fig. 3e shows the C 1s XPS spectra of bitu@C, suggesting a high content of both COOH groups and C–O groups. The fitting results for the O 1s XPS spectra of CB, aCB, and bitu@C are displayed in Fig. S9,† in accordance with the increase in C–O containing groups. Thus, an illustrative structure model for bitu@C is proposed and displayed in Fig. 3f.

Considering that CB, aCB, and bitu@C possess a similar crystalline structure and graphitization degree, the varied electrochemical performances thereby should be attributed to the OFGs. Therefore, the OFGs in bitu@C were further modulated to provide insights into the enhanced $3e^-$ ORR performance. The as-prepared bitu@C samples were annealed under an argon atmosphere at 300 and 800 °C, and the obtained samples were denoted as bitu@C-300 and bitu@C-800, respectively. The results in Fig. 4a indicate that the AOII degradation performance of bitu@C is enhanced after the annealing treatment, while bitu@C-800 exhibits slightly superior performance to bitu@C-300. Similar results are obtained using ITO glass as the substrate (Fig. 4b). The stability of the catalysts is evaluated by refreshing the electrolyte every 30 min. The results in Fig. S10† suggest decent stability of bitu@C, bitu@C-300, and bitu@C-800. Fig. 4c and d show the results for RRDE measurement and the $2e^-$ ORR selectivity, and the electrochemical H_2O_2 activation performance is shown in Fig. 4e. Both the overall ORR current and the $2e^-$ ORR selectivity are decreased after the annealing treatment; however, the H_2O_2 activation performance is enhanced, which might be the primary reason for the enhanced AOII degradation performance. Moreover, the $^{\cdot}OH$ generation during the reaction is evaluated using terephthalate (TPA) as the probe molecule.[54] The catalysts were held at the same working current, and the fluorescent product hydroxyterephthalate (hTPA) was detected. The results in Fig. S11† suggest enhanced $^{\cdot}OH$ production selectivity of bitu@C-300 and bitu@C-800 compared with bitu@C. Furthermore, the electron transfer number of the reaction using different electrocatalysts is evaluated based on the Koutecky–Levich (K–L) equation,[55] and the results are shown in Fig. 4f. At a working potential of 0.2 V, the electron transfer number for bitu@C is 3.5, suggesting that the $4e^-$ ORR accounts for a large proportion of the overall ORR current.

Fig. S12† shows the XRD patterns, and bitu@C-300 and bitu@C-800 exhibit a similar structure to bitu@C. The TG and DTG curves are displayed in Fig. 5a and b. The overall mass loss is 16.7% and 4.0% for bitu@C-300 and bitu@C-800, and the removal of adsorbed water contributes 11.7% and 2.3%, respectively. In the DTG curves, bitu@C-300 shows merely a small peak at around 350 °C, indicating that the content of COOH groups is substantially decreased as compared with that of bitu@C. As for bitu@C-800, the annealing treatment at 800 °C removes most OFGs, and therefore the sample exhibits a constantly low decomposition rate in the temperature range of 300–800 °C without the COOH removal peak. The N_2 adsorption–desorption isotherm curves are shown in Fig. S13.† The sample exhibits slightly enhanced S_{BET} after the removal of surface OFGs (Table S2†). Raman spectra in Fig. 5c also

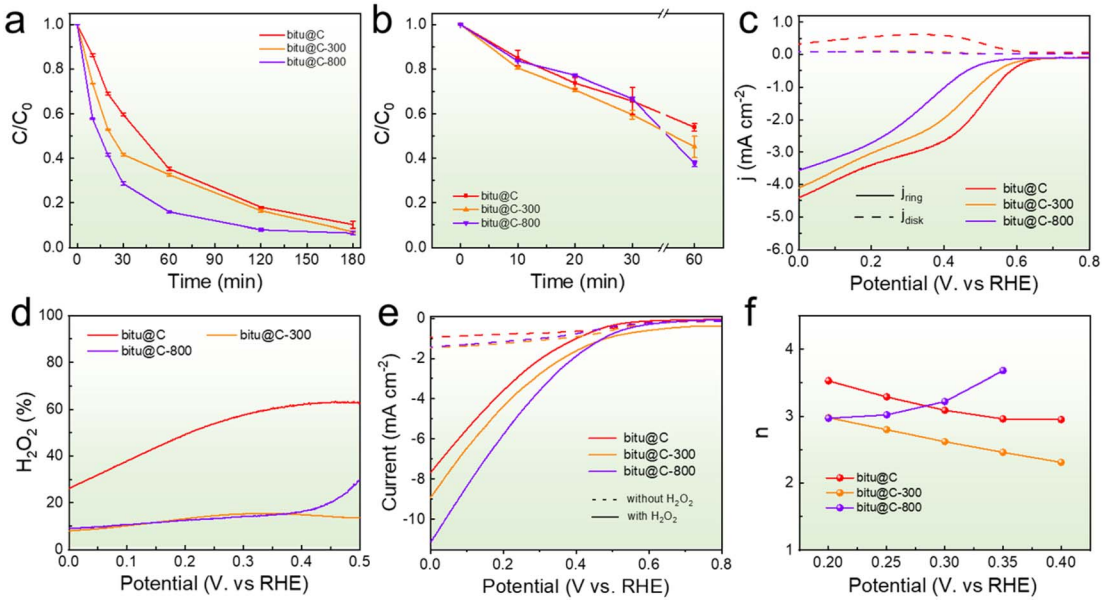

Fig. 4 Electrochemical performance of bitu@C, bitu@C-300, bitu@C-800, and Ni-bitu@C. (a) Degradation of AOII by the $3e^-$ ORR with catalyst loading on carbon cloth, and error bars are based on standard errors. (b) Degradation of AOII by the $3e^-$ ORR with catalyst loading on conductive glass. (c) The polarization curves of the samples measured by using a RRDE. (d) The calculated selectivity toward the $2e^-$ ORR based on the polarization curves. (e) Polarization curves for H_2O_2 electrochemical activation. (f) The calculated electron transfer number at various electrode potentials.

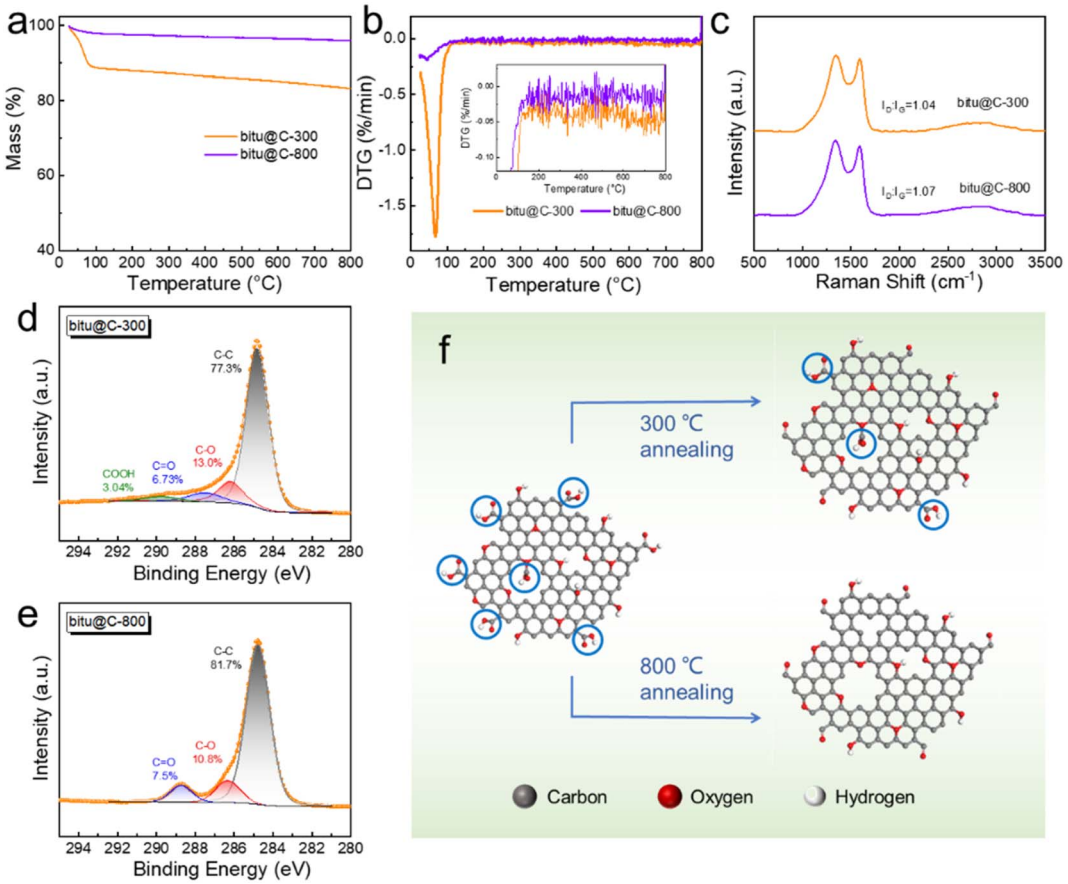

Fig. 5 Structure characterization of the samples. (a) TGA, (b) DTG, and (c) Raman spectra of bitu@C-300 and bitu@C-800. (d and e) High-resolution C 1s XPS spectra of (d) bitu@C-300 and (e) bitu@C-800. (f) Illustration of the structure change in bitu@C after annealing.

demonstrate a similar graphitization degree for bitu@C-300 and bitu@C-800. The C 1s XPS spectra of bitu@C-300 and bitu@C-800 are displayed in Fig. 5d and e, and the corresponding O 1s XPS spectra are shown in Fig. S14.† The fitting results show decreased C–O, C=O, and COOH species in bitu@C-300, consistent with the partial decomposition of COOH groups. As for bitu@C-800, the shoulder peak between 289 and 291 eV disappeared, and the relative ratio of C=O species is somewhat increased. Such a structure variation can be ascribed to the decomposition of COOH that leads to the formation of additional C=O species, as illustrated in Fig. 5f.

Furthermore, theoretical calculations based on the density functional theory (DFT) are employed to explore the role of OFGs in the $3e^-$ ORR process. Fig. 6a displays the ΔG_{OOH*} of various active sites, and the corresponding models are illustrated in Fig. 6b. The COOH groups possess a higher ΔG_{OOH*} as compared with C=O and –OH groups. In general, for the reduction of O_2 to H_2O_2, a high ΔG_{OOH*} indicates that the product can readily desorb from the catalyst and the reaction is controlled by the activation of O_2.[17] In contrast, a low ΔG_{OOH*} indicates that the catalyst binds OOH* strongly and the reaction kinetics is limited by the desorption of H_2O_2. Moreover, the free energy for the H_2O_2 activation process is also calculated. As illustrated in Fig. 6c, the one-electron reduction of H_2O_2 to produce $^{\bullet}OH$ rather than H_2O_2 desorption is more favorable on C=O sites. In contrast, the H_2O_2 desorption process is more favorable on COOH sites (Fig. 6d), and hence the produced H_2O_2 can readily desorb from the catalyst before further activation to $^{\bullet}OH$. Therefore, the above results can fully account for the $3e^-$ ORR performance of the catalysts. The OFG content is low for CB and aCB, leading to an unsatisfactory AOII degradation performance. The bitu@C achieved a high oxygen content of up to 18.8% and hence exhibited a high overall ORR activity. Moreover, the increased COOH groups in bitu@C promote the rapid desorption of H_2O_2 molecules, resulting in decreased selectivity toward the $2e^-$ ORR. The annealing treatment induced the conversion of COOH to C=O groups, and therefore the H_2O_2 activation kinetics is accelerated.

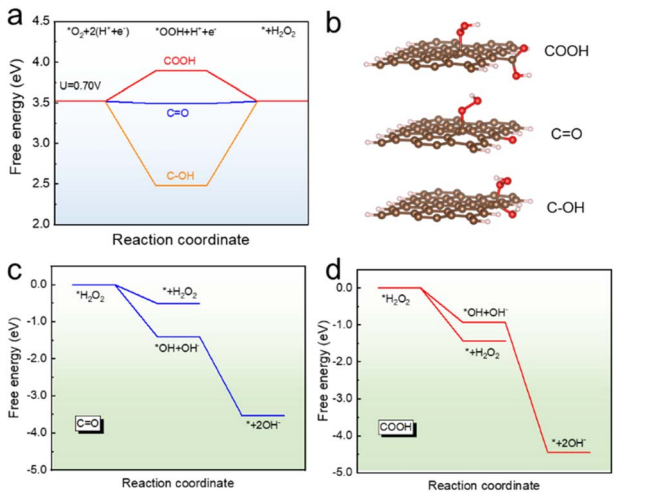

Fig. 6 Theoretical calculation of the samples. (a) Free energy diagrams of the $2e^-$ ORR for different OFGs. (b) The structure for the calculation. Free energy diagrams of H_2O_2 activation and H_2O_2 desorption for (c) C=O and (d) COOH.

4 Conclusions

To sum up, oxygen-rich carbon-based electrocatalysts have been prepared using low-cost bituminous coal as the raw material, and the OFGs in the electrocatalyst are modulated to explore the role of OFGs in the $3e^-$ ORR. The as-prepared bitu@C possessed a high content of OFGs including COOH and C–O–C groups, and the catalyst exhibits more balanced electrochemical H_2O_2 production and activation activity compared with CB and aCB, which enables the efficient production of $^{\bullet}OH$ and the rapid degradation of AOII. Moreover, the H_2O_2 electrochemical activation performance and the contaminant removing efficiency of bitu@C are promoted after an annealing treatment, which induces the conversion of COOH to C=O groups. Theoretical results prove that COOH groups are conducive to the H_2O_2 desorption process, while the H_2O_2 activation process is kinetically more favored at C=O sites. Our work not only demonstrates a straightforward method for synthesizing oxygen-rich carbon-based electrocatalysts but also reveals the crucial role of OFGs in carbon-based electrocatalysts for the $2e^-$ ORR and H_2O_2 activation. The results would provide a fundamental basis and practical techniques for green and efficient organic contaminant removal and are particularly valuable for realizing a green society in the future.

Author contributions

Guoqiang Zhao: conceptualization, funding acquisition, investigation, data curation, methodology, writing – original draft, writing – review & editing. Tianci Chen: data curation, investigation, methodology, validation. Aidong Tang: supervision, project administration, writing – review & editing. Huaming Yang: supervision, project administration, funding acquisition, writing – review & editing.

Conflicts of interest

There are no conflicts to declare.

Acknowledgements

This work was financially supported by the National Natural Science Foundation of China (52301293 and 51974367), the "CUG Scholar" Scientific Research Funds at China University of Geosciences (Wuhan) (Project no. 2022124), the Natural Science Foundation of Hubei Province (No. 2023AFB584), and the Fundamental Research Funds for the Central Universities at China University of Geosciences (Wuhan). G. Zhao acknowledges the financial support from the Natural Science Foundation of Zhejiang Province (LQ22B030005). The authors thank BL10B in NSRL for characterization by synchrotron radiation.

Notes and references

1 S. Rojas and P. Horcajada, *Chem. Rev.*, 2020, **120**, 8378–8415.
2 M. Peydayesh, M. K. Suter, S. Bolisetty, S. Boulos, S. Handschin, L. Nyström and R. Mezzenga, *Adv. Mater.*, 2020, **32**, 1907932.
3 F. Lu and D. Astruc, *Coord. Chem. Rev.*, 2020, **408**, 213180.
4 Y. Dai, N. Zhang, C. Xing, Q. Cui and Q. Sun, *Chemosphere*, 2019, **223**, 12–27.
5 R. Andreozzi, V. Caprio, A. Insola and R. Marotta, *Catal. Today*, 1999, **53**, 51–59.
6 M. Priyadarshini, I. Das, M. M. Ghangrekar and L. Blaney, *J. Environ. Manage.*, 2022, **316**, 115295.
7 L. Chen, J. Duan, P. Du, W. Sun, B. Lai and W. Liu, *Water Res.*, 2022, **221**, 118747.
8 X. Dong, Z. Chen, A. Tang, D. D. Dionysiou and H. Yang, *Adv. Funct. Mater.*, 2022, **32**, 2111565.
9 J. Zhang, Z. Zhou, Z. Feng, H. Zhao and G. Zhao, *Environ. Sci. Technol.*, 2022, **56**, 1331–1340.
10 J. Scaria and P. V. Nidheesh, *Curr. Opin. Chem. Eng.*, 2022, **36**, 100830.
11 E. Oliveros, O. Legrini, M. Hohl, T. Müller and A. M. Braun, *Chem. Eng. Process.*, 1997, **36**, 397–405.
12 J. Wang and J. Tang, *Chemosphere*, 2021, **276**, 130177.
13 S. Zhang, T. Hedtke, Q. Zhu, M. Sun, S. Weon, Y. Zhao, E. Stavitski, M. Elimelech and J.-H. Kim, *Environ. Sci. Technol.*, 2021, **55**, 9266–9275.
14 Z. Wang, M. Liu, F. Xiao, G. Postole, H. Zhao and G. Zhao, *Chin. Chem. Lett.*, 2022, **33**, 653–662.
15 C. D. Gamarra-Güere, D. Dionisio, G. O. S. Santos, M. R. V. Lanza and A. de Jesus Motheo, *J. Environ. Chem. Eng.*, 2022, **10**, 106992.
16 F. Xiao, Z. Wang, J. Fan, T. Majima, H. Zhao and G. Zhao, *Angew. Chem., Int. Ed.*, 2021, **60**, 10375–10383.
17 L. Xie, P. Wang, W. Zheng, S. Zhan, Y. Xia, Y. Liu, W. Yang and Y. Li, *Proc. Natl. Acad. Sci. U. S. A.*, 2023, **120**, e2307989120.
18 C. Xia, Y. Xia, P. Zhu, L. Fan and H. Wang, *Science*, 2019, **366**, 226–231.
19 G. O. Santos, P. J. Cordeiro Junior, I. Sánchez Montes, R. S. Souto, M. S. Kronka and M. R. Lanza, *Curr. Opin. Electrochem.*, 2022, 101124.
20 Y. Wen, T. Zhang, J. Wang, Z. Pan, T. Wang, H. Yamashita, X. Qian and Y. Zhao, *Angew. Chem., Int. Ed.*, 2022, **61**, e202205972.
21 Y. Wang, G. I. Waterhouse, L. Shang and T. Zhang, *Adv. Energy Mater.*, 2021, **11**, 2003323.
22 X. Zhang, H. Su, P. Cui, Y. Cao, Z. Teng, Q. Zhang, Y. Wang, Y. Feng, R. Feng and J. Hou, *Nat. Commun.*, 2023, **14**, 7115.
23 Z. Wang, F. Xiao, X. Shen, D. Zhang, W. Chu, H. Zhao and G. Zhao, *Environ. Sci. Technol.*, 2022, **56**, 13740–13750.
24 D. J. Kim, Q. Zhu, K. Rigby, X. Wu, J. H. Kim and J.-H. Kim, *Environ. Sci. Technol.*, 2022, **56**, 1365–1375.
25 Z. Lu, G. Chen, S. Siahrostami, Z. Chen, K. Liu, J. Xie, L. Liao, T. Wu, D. Lin and Y. Liu, *Nat. Catal.*, 2018, **1**, 156–162.
26 H. W. Kim, M. B. Ross, N. Kornienko, L. Zhang, J. Guo, P. Yang and B. D. McCloskey, *Nat. Catal.*, 2018, **1**, 282–290.
27 Y. Bu, Y. Wang, G.-F. Han, Y. Zhao, X. Ge, F. Li, Z. Zhang, Q. Zhong and J.-B. Baek, *Adv. Mater.*, 2021, **33**, 2103266.
28 Y. Wang, R. Shi, L. Shang, G. I. Waterhouse, J. Zhao, Q. Zhang, L. Gu and T. Zhang, *Angew. Chem., Int. Ed.*, 2020, **59**, 13057–13062.
29 Y. Guo, R. Zhang, S. Zhang, H. Hong, Y. Zhao, Z. Huang, C. Han, H. Li and C. Zhi, *Energy Environ. Sci.*, 2022, **15**, 4167–4174.
30 E. Jung, H. Shin, B.-H. Lee, V. Efremov, S. Lee, H. S. Lee, J. Kim, W. Hooch Antink, S. Park, K.-S. Lee, S.-P. Cho, J. S. Yoo, Y.-E. Sung and T. Hyeon, *Nat. Mater.*, 2020, **19**, 436–442.
31 F. Xiang, X. Zhao, J. Yang, N. Li, W. Gong, Y. Liu, A. Burguete-Lopez, Y. Li, X. Niu and A. Fratalocchi, *Adv. Mater.*, 2023, **35**, 2208533.
32 K. Lian, Q. Wan, R. Jiang and S. Lin, *Catalysts*, 2023, **13**, 307.
33 M. Mazzucato and C. Durante, *Curr. Opin. Electrochem.*, 2022, 101051.
34 F. Yang, X. Ma, W.-B. Cai, P. Song and W. Xu, *J. Am. Chem. Soc.*, 2019, **141**, 20451–20459.
35 V. Datsyuk, M. Kalyva, K. Papagelis, J. Parthenios, D. Tasis, A. Siokou, I. Kallitsis and C. Galiotis, *Carbon*, 2008, **46**, 833–840.
36 C. Tang, L. Chen, H. Li, L. Li, Y. Jiao, Y. Zheng, H. Xu, K. Davey and S.-Z. Qiao, *J. Am. Chem. Soc.*, 2021, **143**, 7819–7827.
37 K.-H. Wu, D. Wang, X. Lu, X. Zhang, Z. Xie, Y. Liu, B.-J. Su, J.-M. Chen, D.-S. Su, W. Qi and S. Guo, *Chem*, 2020, **6**, 1443–1458.
38 S. Siahrostami, A. Verdaguer-Casadevall, M. Karamad, D. Deiana, P. Malacrida, B. Wickman, M. Escudero-Escribano, E. A. Paoli, R. Frydendal and T. W. Hansen, *Nat. Mater.*, 2013, **12**, 1137–1143.
39 S. Lu, L. Liu, H. Demissie, G. An and D. Wang, *Environ. Int.*, 2021, **146**, 106273.
40 S. Hussain, E. Aneggi and D. Goi, *Environ. Chem. Lett.*, 2021, **19**, 2405–2424.
41 N. Thomas, D. D. Dionysiou and S. C. Pillai, *J. Hazard. Mater.*, 2021, **404**, 124082.
42 G. Kresse and J. Furthmüller, *Phys. Rev. B: Condens. Matter Mater. Phys.*, 1996, **54**, 11169.
43 P. E. Blöchl, *Phys. Rev. B: Condens. Matter Mater. Phys.*, 1994, **50**, 17953.
44 J. P. Perdew, K. Burke and M. Ernzerhof, *Phys. Rev. Lett.*, 1996, **77**, 3865.
45 Y. Zhu, S. Murali, M. D. Stoller, K. J. Ganesh, W. Cai, P. J. Ferreira, A. Pirkle, R. M. Wallace, K. A. Cychosz and M. Thommes, *Science*, 2011, **332**, 1537–1541.
46 J. Zhang, H. Zhou, X. Liu, J. Zhang, T. Peng, J. Yang, Y. Huang and S. Mu, *J. Mater. Chem. A*, 2016, **4**, 15870–15879.
47 N. Y. Donkadokula, A. K. Kola, I. Naz and D. Saroj, *Rev. Environ. Sci. Bio/Technol.*, 2020, **19**, 543–560.
48 X. Shi, S. Back, T. M. Gill, S. Siahrostami and X. Zheng, *Chem*, 2021, **7**, 38–63.

49 L. Li, X. Yao, H. Li, Z. Liu, W. Ma and X. Liang, *J. Chem. Eng. Jpn.*, 2014, **47**, 21–27.
50 G. S. Szymański, Z. Karpiński, S. Biniak and A. Świątkowski, *Carbon*, 2002, **40**, 2627–2639.
51 K. H. Kangasniemi, D. Condit and T. Jarvi, *J. Electrochem. Soc.*, 2004, **151**, E125.
52 Z. Zhang, L. Pfefferle and G. L. Haller, *Chin. J. Catal.*, 2014, **35**, 856–863.
53 A. Kuznetsova, I. Popova, J. T. Yates, Jr., M. J. Bronikowski, C. B. Huffman, J. Liu, R. E. Smalley, H. H. Hwu and J. G. Chen, *J. Am. Chem. Soc.*, 2001, **123**, 10699–10704.
54 E. M. Rodríguez and U. von Gunten, *Water Res.*, 2020, **177**, 115691.
55 Y. Chen, X. Zheng, J. Cai, G. Zhao, B. Zhang, Z. Luo, G. Wang, H. Pan and W. Sun, *ACS Catal.*, 2022, **12**, 7406–7414.